

# Sunflower Pollen-Morphology Mimicked Spiky Zinc Nanomotors as a Photosensitizer for Killing Bacteria and Cancer Cells

Sayan Deb Dutta,<sup>#</sup> Rachmi Luthfikasari,<sup>#</sup> Tejal V. Patil,<sup>#</sup> Keya Ganguly, Youjin Seol, Aayushi Randhawa, and Ki-Taek Lim<sup>\*</sup>



Cite This: <https://doi.org/10.1021/acsabm.4c00092>



Read Online

ACCESS |



Metrics & More



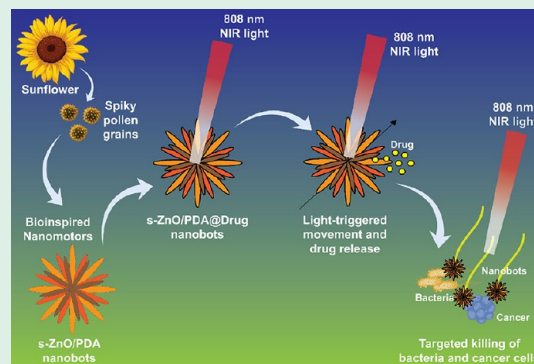
Article Recommendations



Supporting Information

**ABSTRACT:** Photosensitizing agents have received increased attention from the medical community, owing to their higher photothermal efficiency, induction of hyperthermia, and sustained delivery of bioactive molecules to their targets. Micro/nanorobots can be used as ideal photosensitizing agents by utilizing various physical stimuli for the targeted killing of pathogens (e.g., bacteria) and cancer cells. Herein, we report sunflower-pollen-inspired spiky zinc oxide (s-ZnO)-based nanorobots that effectively kill bacteria and cancer cells under near-infrared (NIR) light irradiation. The as-fabricated s-ZnO was modified with a catechol-containing photothermal agent, polydopamine (PDA), to improve its NIR-responsive properties, followed by the addition of antimicrobial (e.g., tetracycline/TCN) and anticancer (e.g., doxorubicin/DOX) drugs. The fabricated s-ZnO/PDA@Drug nanorobots exhibited unique locomotory behavior with an average speed ranging from 13 to 14  $\mu\text{m/s}$  under 2.0  $\text{W/cm}^2$  NIR light irradiation. Moreover, the s-ZnO/PDA@TCN nanorobots exhibited superior antibacterial activity against *E. coli* and *S. epidermidis* under NIR irradiation. The s-ZnO/PDA@DOX nanorobots also displayed sufficient reactive oxygen species (ROS) amplification in B16F10 melanoma cells and induced apoptosis under NIR light, indicating their therapeutic efficacy. We hope the sunflower pollen-inspired s-ZnO nanorobots have tremendous potential in biomedical engineering from the phototherapy perspective, with the hope to reduce pathogen infections.

**KEYWORDS:** photosensitizers, nanorobots, zinc oxide, photothermal therapy, reactive oxygen species



## 1. INTRODUCTION

Localized delivery of chemotherapeutic drugs remains challenging for the medical community in combating pathogenic (e.g., bacteria and mold) infections and cancers. The conventional strategy involves the untargeted delivery and bioaccumulation of chemical drugs, leading to serious side effects in the human body. Micro/nanoscale robots have recently received tremendous attention to address this issue.<sup>1</sup> Micro/nanorobots are small-scale tiny and biocompatible robots with versatile functionalities.<sup>2,3</sup> The use of micro/nanorobots has been increasing rapidly in the medical community owing to their ability to deliver various therapeutic molecules (e.g., growth factors) and drugs with tailorable surface functionalities, unprecedented motility, and tissue penetration abilities for targeted therapy.<sup>3</sup> These micro/nanomotors can be manipulated via the application of various biophysical stimuli, such as electric field,<sup>4–6</sup> magnetic field,<sup>7,8</sup> ultrasound,<sup>9–11</sup> or light<sup>8,12–14</sup> stimuli.

Light or photoresponsive micro/nanorobots have been widely explored over the past few years. Light is a particularly powerful source of micro/nanobot locomotion owing to its renewable, cost-effective, and noninvasive nature.<sup>15</sup> To fuel micro/nanobots using light, the structural composition must be considered. Light-responsive photocatalytic nanomaterials can be used as

energy-harvesting sources to generate motion in robots. For example, multimaterial Janus micro/nanobots with photocatalytic properties, such as UV-light-activated  $\text{TiO}_2$  and  $\text{ZnO}$  nanostructures and visible-light-activated  $\text{Fe}_2\text{O}_3$  and bibased nanostructures having a metal coating, could be used as ideal light-fueled microbots for therapeutic applications.<sup>15</sup> Apart from UV and visible light, near-infrared (NIR) can also be used as a fuel source for NIR-responsive micro/nanobots.<sup>16</sup> The NIR-triggered micro/nanobots not only act as a fuel source, but also behave as a photosensitizer, which induces local hyperthermia and reactive oxygen species (ROS) for targeted killing of pathogen and tumor cells.<sup>17–20</sup>

Artificial micro- and nanobots have been developed for various biomedical applications inspired by natural biological motors. For example, pollen and plant spores have emerged as potential materials for drug delivery and could be used as

**Received:** January 21, 2024

**Revised:** May 24, 2024

**Accepted:** May 29, 2024

catalysts owing to their biocompatibility, resistance to acids and alkalis, and ability to withstand high temperatures.<sup>21</sup> However, when using chemical fuels, such as hydrogen peroxide (H<sub>2</sub>O<sub>2</sub>),<sup>22</sup> micro/nanobots exhibit potential toxicity to animal cells due to the amplification of ROS. Consequently, various biocompatible fuel sources, such as glucose, urea, and water, were relatively biocompatible.<sup>23</sup> Song et al.<sup>2</sup> reported that microbots from *Chrysanthemum* flower pollen exhibited excellent motility owing to the presence of a light source. This platform proved that biomimetic materials with light as a power source are highly biocompatible and promising for future biomedical applications. Due to their unique spiky structures, pollen grains with various micro/nanostructures are promising candidates for micro/nanobot fabrication. In addition, there are several limitations to using pollen-based micro/nanobots, such as size variability, limited payload and degradability, immune response triggering, and standardization and quality control challenges. However, zinc oxide (ZnO) nanoparticles (NPs) have recently attracted considerable attention because of their various structural functionalities that can be tailored by regulating specific chemical reactions. Spike-shaped micro/nanoparticles offer several advantages over smooth surfaces. For example, utilizing a smaller spike shape enables enhanced deep penetration, increased drug encapsulation, improved catalytic activity, enhanced light absorption, more excellent stability, customizable properties, and easier control for the fabrication of micro/nanobots.<sup>24</sup> Dang et al.<sup>25</sup> successfully demonstrated the role of spiky ZnO (s-ZnO) NPs with outstanding anticancer properties. This finding indicates that s-ZnO NPs are ideal micro- and nanobot fabrication materials.

In this study, we fabricated light-responsive nanobots inspired by sunflower pollen featuring a spiky ZnO/PDA composition designed for bacterial eradication and cancer cell killing. The fabrication involved the synthesis of ZnO particles with spiky structures, which were subsequently coated with polydopamine (PDA) to enhance the photosensitivity of the resulting s-ZnO/PDA robots. Additionally, we synthesized round ZnO/PDA nanoparticles to compare their structural differences with those of the spiky structures. The drug-loaded nanobots exhibited remarkable bactericidal and cancer-inhibitory effects under near-infrared (NIR) light exposure. External control using an 808 nm NIR light facilitated the activation and steering of these nanobots. In addition, the particles demonstrated substantial photothermal efficiency at 2.0 W/cm<sup>2</sup>, ensuring their mobility and effective killing activity. This conceptualization of the s-ZnO/PDA@Drug nanobot design serves as a facile fabrication, NIR responsive propulsion, and effective drug delivery to the target and is capable of executing diverse tasks within a single nanobot structure.

## 2. EXPERIMENTAL SECTION

**2.1. Materials.** Zinc nitrate hexahydrate (Zn(NO<sub>3</sub>)<sub>2</sub>·6H<sub>2</sub>O, purity > 98%) was purchased from Thermo-Fischer Scientific, U.S.A. Dopamine hydrochloride, tetracycline hydrochloride (TCN), doxorubicin hydrochloride (DOX, purity > 99%) were obtained from Sigma-Aldrich, U.S.A. Sodium hydroxide (NaOH, purity > 98%) was purchased from Alfa Aesar, France. Hydroxylamine hydrochloride (NH<sub>2</sub>OH·HCl, purity > 97%) and sodium chlorite (NaClO<sub>2</sub>, purity > 99%) was provided by Daejung, Republic of Korea. Glutaraldehyde was obtained from Fischer Bioreagents, U.S.A. All of the chemicals were used without any further modification unless stated elsewhere. Milli-Q water (18.2 mΩ·cm<sup>-1</sup>@25 °C) was used for the dissolution of all chemicals.

**2.2. Synthesis and Characterization of s-ZnO and r-ZnO.** s-ZnO nanoparticles were synthesized according to a previously reported method with minor modifications.<sup>25</sup> Briefly, 2.84 g of zinc nitrate hexahydrate (0.3 M) and hydroxylamine hydrochloride (0.347 g, 0.1 M) were dissolved in 50 mL of distilled water. Next, a 3 M NaOH solution was prepared and slowly poured into the as-prepared mixture with constant stirring until the pH reached 12. After 30 min of stirring, the aqueous solution was transferred to a refluxing pot, followed by calcination at 90 °C for 20 min. The obtained powder was washed with methanol three times and dried at room temperature to obtain an s-ZnO powder. The crystalline structure of the s-ZnO was analyzed using an X-ray diffractometer (X'Pert Pro MPD, Netherlands) with an operating voltage of 40 kV and Cu K-alpha radiation (λ = 1.541 Å). The morphology of the particles was examined by using field-emission scanning electron microscopy (FE-SEM; Jeol, Japan). The chemical compositions of the synthesized particles were evaluated by using Fourier transform infrared (FT-IR) spectroscopy (Frontier, PerkinElmer, U.K.).

Similarly, r-ZnO nanoparticles were synthesized using a previously reported method with minor modifications.<sup>25</sup> Briefly, 0.8925 g of zinc nitrate hexahydrate (0.06 M) was dissolved in 50 mL of deionized water, and 0.24 g of NaOH (0.12 M) was added dropwise with vigorous stirring. The pH of the solutions was measured at 10, and the mixture was stirred constantly for 5 h. Subsequently, the aqueous precipitate was washed three times with deionized water and calcined at 450 °C for 5 h in an annealing furnace. The r-ZnO powder obtained was stored in a dry place until further use. FE-SEM and EDS characterized the r-ZnO.

**2.2.1. Fabrication of r/s-ZnO/PDA@TCN Nanobots.** The functionalization process was followed according to previous report with minor modifications.<sup>2</sup> Initially, PDA was coated onto the ZnO NPs to prepare the nanobots. ZnO (10 mg), DA-HCl (20 mg), and Tris-HCl (10 mL; pH = 8.5; 5.0 mM) were mixed and reacted under vibration at 200 rpm and 33 °C for 12 h. The product ZnO/PDA was washed with distilled water by centrifugation and dried at room temperature. Subsequently, the ZnO/PDA nanobots (10 mg) was suspended in H<sub>2</sub>O (12 mL) containing glutaraldehyde (GA; 12 μL; 50 wt %). The mixture was then incubated at 45 °C for 1 h to obtain GA-activated ZnO/PDA nanobots and washed with deionized water to remove unbound GA molecules. GA-activated ZnO/PDA nanobots were suspended in 12 mL of tetracycline hydrochloride (1 mg/mL) and incubated at 45 °C for 1 h. The resultant ZnO/PDA@TCN nanobots were rinsed five times with deionized water and dried at room temperature.

**2.2.2. Fabrication of r/s-ZnO/PDA@DOX Nanobots and Drug Loading.** For DOX loading, r/s-ZnO/PDA particles were resuspended in 12 mL of deionized water containing 1.0 mg/mL doxorubicin for 24 h, 100 rpm, at room temperature. The resulting r/s-ZnO/PDA@DOX nanobots were rinsed three times with deionized water and dried at room temperature. The drug encapsulation efficiency was calculated by the given formula:

$$\text{drug encapsulation efficiency(\%)} = \frac{\text{wt of drug in nanoparticles}}{\text{wt of drug in feed}} \times 100$$

The drug concentration was detected by an absorption quantitative standard curve (absorption wavelength for TCN is 357 nm and for DOX is 490 nm).

**2.3. Photothermal Performance.** The photothermal capabilities of s-ZnO and s-ZnO/PDA nanobots were methodically investigated by subjecting the nanofibers to 808 nm NIR laser illumination. Various nanobot concentrations (0.1 and 0.5 mg/mL) were dispersed in water to assess their photothermal characteristics. The real-time temperature was monitored over 5 min with temperature measurements recorded every minute. The photothermal effects of the s-ZnO and s-ZnO/PDA nanobots were examined at laser power densities of 1.0 and 2.0 W/cm<sup>2</sup>.

**2.4. Radical Generation.** Electron spin resonance (ESR) spectra of s-ZnO/PDA were obtained to check radical generation. The analysis was performed with and without NIR irradiation (for 5 min) at room temperature. The sample was prepared at a 0.5 mg/mL concentration, and a 2,2,6,6-tetramethyl-4-piperidone (TEMP) probe was used as the radical trapping agent.

**2.5. Performances of the Nanobots.** First, an aqueous suspension (400  $\mu\text{L}$ , 0.5 mg/mL) containing the s-ZnO/PDA@Drug nanobots was dropped onto a glass slide, and a near-infrared (NIR) laser of the wavelength of 808 nm (FC-808-40 W, Changchun New Industries, China) was irradiated on one side of the glass slide. The motion of the nanobots was observed using an inverted optical microscope (Carl Zeiss Axio Vert. A1, U.S.A.) with 4 $\times$  objective lenses. A high-definition industrial digital camera (Eyecam, Zeiss, U.S.A.) was used to capture and record the motion of the nanobots at 30 frames per second (fps) in phase-contrast mode. All videos were analyzed using the ImageJ v1.52 (<https://imagej.nih.gov/ij/index.html>, NIH, Bethesda, U.S.A.) and Origin Pro v9.0 (Origin Lab Corporation, Northampton, MA, U.S.A.) software.

**2.6. Antibacterial Performance.** *Staphylococcus epidermidis* (ATCC-12228, U.S.A.) and *Escherichia coli* (KCTC-2593, Republic of Korea) were obtained to evaluate the antibacterial performance of s-ZnO/PDA@TCN. The fresh bacteria culture was prepared in nutrient liquid culture medium containing beef extract (3 g/L) and peptone (5 g/L) in an oscillator at 37  $^{\circ}\text{C}$  and 200 rpm and was then harvested at the exponential growth phase. The bacterial concentration was determined by measuring the optical density (OD) at a wavelength of 600 nm. The bacterial suspension was then diluted with media until the OD was 0.1 before starting the experiment. To check the motility of bacteria and our prepared nanobots, 50  $\mu\text{L}$  of each were placed on glass slides. The movement was recorded under the NIR laser irradiation. The antibacterial performance was evaluated in the presence and absence of NIR light. 100  $\mu\text{L}$  of bacteria was added in 500  $\mu\text{g}/\text{mL}$  of s-ZnO/PDA@TCN liquid solutions. The bacteria were incubated with samples for 6 h at 37  $^{\circ}\text{C}$  and 200 rpm conditions. Group without any sample was considered as the control. After 6 h incubation, the samples were irradiated with NIR light (2.0  $\text{W}/\text{cm}^2$ ) for 5 min. 100  $\mu\text{L}$  of  $10^{-4}$  serial diluted bacteria were spread on nutrient agar plates. To conduct fluorescence staining, live–dead assay was performed. Two  $\mu\text{L}$  of SYTO9 (30  $\mu\text{M}$ ) and propidium iodide (10  $\mu\text{M}$ ) fluorescent dyes were added to label live and dead bacterial cells green and red, respectively. Incubation was performed in the dark for 30 min. Next, the stained sample was placed on a glass slide for fluorescence imaging.

**2.7. Evaluation of Anticancer Properties.** **2.7.1. Cell Viability Assay.** B16F10 (ATCC CRL-6475) and human dermal fibroblast (HDF, ATCC No. PCS-201-012) cell lines were selected to examine the cytotoxicity effect anticancer activity of fabricated s-ZnO/PDA@DOX nanobots. B16F10 and HDF cells were cultured in Dulbecco's Modified Eagle Medium (DMEM) supplemented with 10% fetal bovine serum (FBS; Merck Millipore, U.S.A.) and 1% penicillin and streptomycin (Gibco, Grand Island, NY, U.S.A.). Cells were kept in a humidified incubator with 5%  $\text{CO}_2$  at 37  $^{\circ}\text{C}$ . Samples were prepared in deionized water at 1 mg/mL concentration, followed by 24 h of UV sterilization prior to use. The storage solution was vortexed and diluted in DMEM to give a working concentration of 0.5 mg/mL working concentration. For cell viability assessment, B16F10 and HDF cells were seeded onto 96-well plates at  $1 \times 10^4$  cells/well/100  $\mu\text{L}$  and cultured for 24 h. Next, the cells were incubated with s-ZnO and s-ZnO/PDA@DOX for 24 h and then irradiated with NIR light (2.0  $\text{W}/\text{cm}^2$ , 808 nm) for 5 min. After the desired time point, 10  $\mu\text{L}$  of WST-8 dye (Cellrix Viability Assay Kit, Republic of Korea) was added to each well and incubated for 2 h. Viable cells with and without NIR light exposure were assessed by measuring the absorbance at 450 nm with a reference at 625 nm using a microplate reader (Infinite M Nano 200 Pro, TECAN, Switzerland). The percentage of viable cells were calculated according to the given formula:

$$\text{cell viability (\%)} = \frac{\text{absorbance of treatment}}{\text{absorbance of control}} \times 100$$

The results represent the averages of at least three replicates.

**2.7.2. ROS and MitoTracker Red Staining.** The fluorescent probes DCF-DA and MitoTracker (MT) Red were used to determine the levels of reactive oxygen species (ROS) and active mitochondria in the cells. B16F10 cells were seeded in a 48-well plate at a density of  $2.0 \times 10^4$  cells/well and incubated for 24 h at 37  $^{\circ}\text{C}$  with 5%  $\text{CO}_2$  before experiments. S-ZnO/PDA@DOX was exposed to the cells for 24 h.

The cells were then washed with 1 $\times$  M PBS before staining. To detect ROS production, cells were incubated with DCF-DA (10  $\mu\text{M}$ ) at 37  $^{\circ}\text{C}$  for 10 min. Similarly, the cells were incubated with MT Red (10  $\mu\text{M}$ ) at 37  $^{\circ}\text{C}$  for 10 min to detect the active mitochondria. After staining, the cells were washed twice with 1 $\times$  PBS and imaged using a fluorescence microscope (DMI8 series, Leica Microsystems, Germany). Sample was irradiated with NIR light (2.0  $\text{W}/\text{cm}^2$ ) for 5 min and the staining process was repeated under the same conditions.

**2.7.3. Spheroid Culture and Study of Anticancer Performance.** The widely used hanging drop culture technique was used to form cancer cell spheroids. B16F10 cells were seeded and cultured at a density of 200 cells/drop/20  $\mu\text{L}$  and incubated at 37  $^{\circ}\text{C}$  with 5%  $\text{CO}_2$  for at least 3–5 days. The formed spheroids (size:  $\sim 350 \mu\text{m}$ ) were identified based on their size and shape. The fifth day grown spheroids were used for the toxicity studies. The spheroids were incubated with all of the samples for 24 h before imaging. The number and distribution of live and dead cells were assessed by ethidium bromide/acridine orange (EtBr/AO) staining under a fluorescence microscope (Leica Biosystems, Germany). NIR irradiation at 808 nm was applied for 5 min with a laser power density of 2.0  $\text{W}/\text{cm}^2$ .

**2.7.4. Propidium Iodide/Annexin-V Staining.** The apoptosis level in B16F10 cells in the presence of s-ZnO/PDA@DOX w/ or w/o NIR is evaluated using the propidium iodide/Annexin-V staining. Briefly,  $2.5 \times 10^4$  cells were seeded onto the 6-well plates and incubated for 48 h. After 48 h, the cells were treated with 0.5 mg/mL s-ZnO/PDA@DOX and further incubated for 2–4 h. After that, the cells were irradiated with 2.0  $\text{W}/\text{cm}^2$  NIR light (808 nm) for 5 min. Next, the cells were washed with 1 $\times$  PBS and harvested in 500  $\mu\text{L}$  of staining solution. The cells were incubated for 30 min in ice and analyzed using a FACS Calibur instrument (BD Bioscience, NJ, U.S.A.) with appropriate filter channels. The data was processed with BD FACS Diva v9.1 (BD Bioscience, NJ, U.S.A.). The samples without NIR and s-ZnO/PDA@DOX were also assessed to compare the apoptosis level.

**2.7.5. Cellular Uptake Study.** B16F10 cells and spheroids were cultured with s-ZnO/PDA@DOX for 24 h to assess nanobot uptake. After incubation, the cells were fixed with 4% paraformaldehyde for 20 min, followed by DAPI staining for 5 min. DOX was excited at 470 nm and emitted a signal at 595 nm which can be visualized in the red channel of fluorescence microscope. Consequently, the conjugation of DOX with nanoparticles allowed for visualization of red fluorescence. Thus, fluorescence microscopy was used to study the uptake of s-ZnO/PDA@DOX by cells and spheroids. The photographs were analyzed using ImageJ (v1.8, NIH, Bethesda, U.S.A.) software, and a colocalization test was carried out to ensure the nuclear accumulation of nanobots, as reported in our previous study.<sup>26</sup>

**2.7.6. Immunogenic Response of Nanobots.** Murine monocyte cells (RAW 264.7) were cultured in a 24-well plate at a density of  $2 \times 10^4$  cells per well and incubated at 37  $^{\circ}\text{C}$  overnight before the experiments. The cells were then exposed to 0.5 mg/mL of s-ZnO/PDA@DOX nanobots for 24 h. For qRT-PCR analysis, the cells were harvested using the TRIzol reagent to extract RNA, which was then purified. Subsequently, cDNA was synthesized using SuperScript Reverse Transcriptase IV, followed by qRT-PCR. The expression of M2 polarization genes, including *CD163*, *IL-4*, and *VEGF*, was investigated. Immunocytochemistry (ICC) was conducted to assess the *CD163* and *iNOS* protein expression in cells after s-ZnO/PDA@DOX treatment. Additional information on the PCR and ICC procedures can be found in Supporting Information.

**2.8. Statistical Analysis.** Statistical analysis was performed using Origin Pro v9.1 (Origin Laboratories, U.S.A.) for all the experiments. The significant difference between the control and treatment group was assessed using One-way Analysis of Variance (ANOVA) test. Data reported in this study are mean  $\pm$  s.d. of triplicate ( $n = 3$ ) experiments, statistical significance at \* $p < 0.05$ , \*\* $p < 0.01$ , and \*\*\* $p < 0.001$ .

## 3. RESULTS AND DISCUSSION

**3.1. Characterization of the s-ZnO and r-ZnO Nanobots.** Photoresponsive and drug-loaded s-ZnO and r-ZnO nanobots were fabricated through the reaction of ZnO

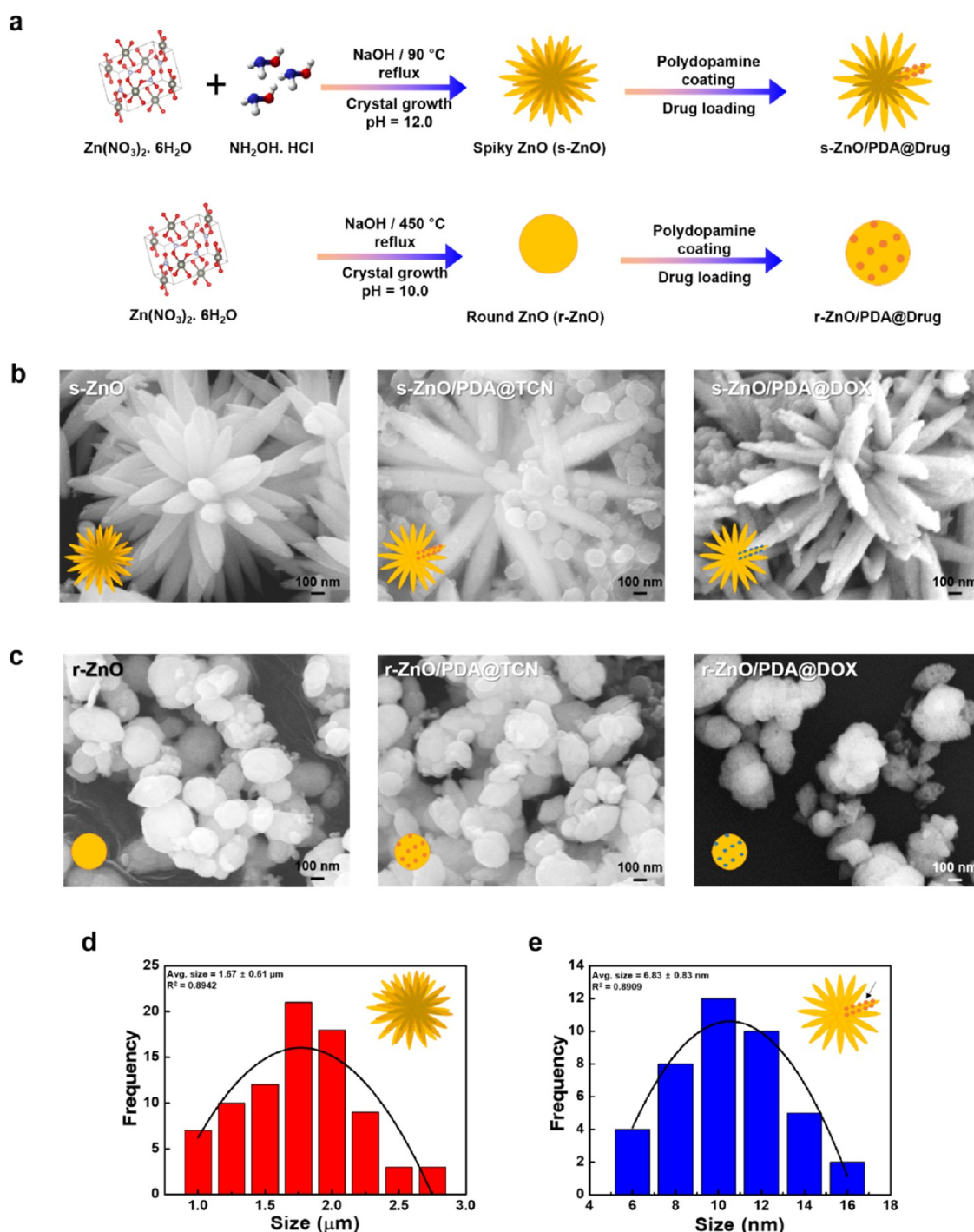


**Figure 1.** (a) Schematic illustration of the sunflower pollen-inspired spiky ZnO (s-ZnO) nanorobots fabrication. (b) FE-SEM images of the spiky (s-) and (c) round (r-) ZnO, ZnO/PDA@TCN, and ZnO/PDA@DOX. Scale bar: 100 nm. (d) Size distribution graph of the s-ZnO nanoflowers and (e) TCN nanoparticles in the s-ZnO/PDA@TCN. The black arrow indicates the TCN nanoparticle location onto the s-ZnO/PDA surface.

particles with PDA, followed by the immobilization of suitable drugs to enhance therapeutic efficiency. Figure 1a schematically shows the fabrication procedure for the motile ZnO nanobots. PDA was deposited onto the ZnO surface via oxidative polymerization of DA in an alkaline medium. The morphological and structural features of pure ZnO and its composites were evaluated using FE-SEM and FTIR spectroscopy and compared (structure) with those of natural sunflower pollen. As shown in Figure S1, the raw sunflower pollen exhibits a unique spiky morphology (spike length: 3–5  $\mu\text{m}$ ) with a spherical core

having a diameter of  $35\text{--}40 \pm 0.25 \mu\text{m}$ .<sup>27,28</sup> Besides, the s-ZnO showed clustered nanostructures with spine-shaped nanorods having a diameter of  $1.67 \pm 0.61 \mu\text{m}$ , protruding from the base (Figure 1b,d). The r-ZnO exhibited a smooth-surfaced, round-shaped morphology (Figure 1c). In the basic medium (pH 12.0),  $\text{Zn}(\text{NO}_3)_2$  was converted into zincate ions  $[\text{Zn}(\text{OH})_4]^{2-}$ , which further contributed to the crystal growth phase of s-ZnO during refluxing at high temperatures.<sup>25</sup> The presence of  $\text{NH}_2\text{OH}\cdot\text{HCl}$  induces the crystal growth of s-ZnO nanospikes and produces a small amount of hydroxyl ions, which is crucial

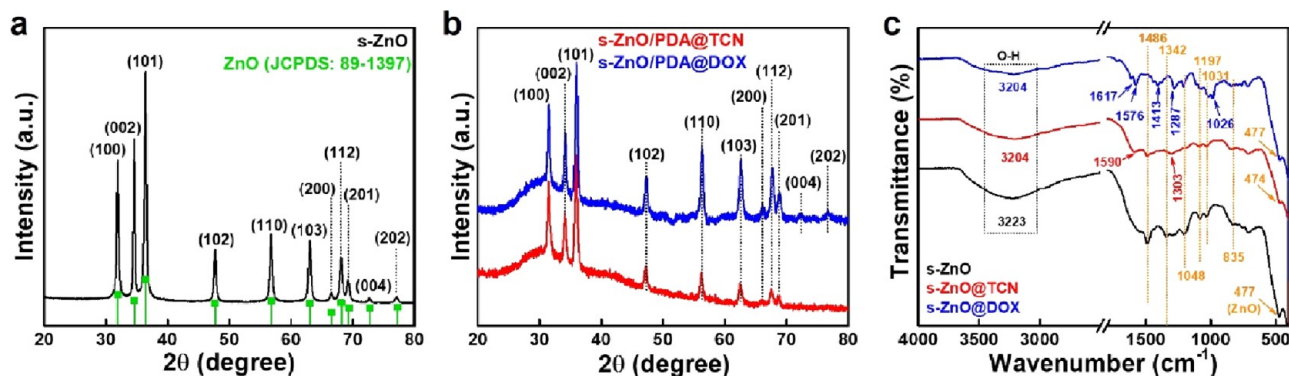


**Figure 2.** (a) XRD spectra of the ZnO standard (JCPDS: 89-1397) and s-ZnO nanoflowers. (b) XRD spectra of the s-ZnO/PDA@TCN and s-ZnO/PDA@DOX. (c) FT-IR spectra of the s-ZnO, s-ZnO/PDA@TCN, and s-ZnO/PDA@DOX.

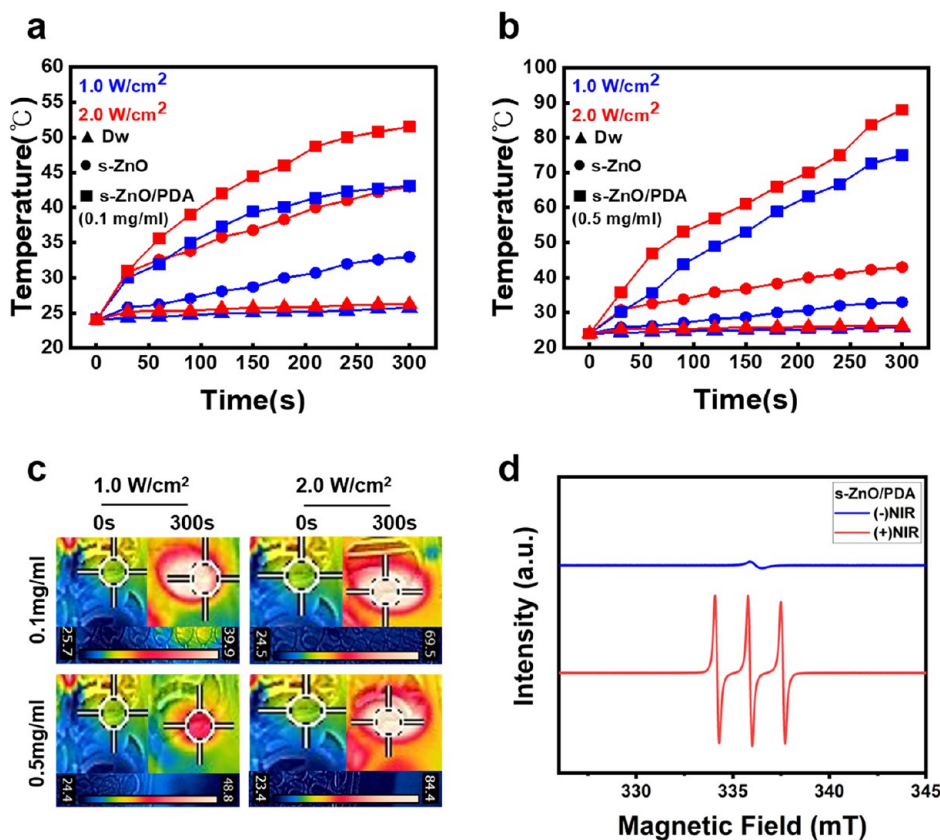


**Figure 3.** Photothermal properties of distilled water (D.W.), s-ZnO, and s-ZnO/PDA nanobots. Change in temperature as a function of time of the nanobots at a concentration of (a) 0.1 and (b) 0.5 mg/mL under 1.0 and 2.0 W/cm<sup>2</sup> NIR light (808 nm) irradiation. (c) Representative thermal images of the heat generation from 0 to 300 s (5 min) of s-ZnO/PDA. (d) ESR spectra of s-ZnO/PDA w/ or w/o NIR showing the <sup>1</sup>O<sub>2</sub> radical generation *in vitro*.

for controlling the self-assembly of Zn. The absence of NH<sub>2</sub>OH·HCl resulted in the fabrication of round-shaped ZnO, referred to as r-ZnO. Low-resolution FE-SEM images of pure r/s-ZnO, r/s-ZnO/PDA@TCN, and r/s-ZnO/PDA@DOX are shown in Figure S2. Olsson et al.<sup>29</sup> reported ZnO nanoneedle-like nanoclusters through controlling the concentration of NaOH with a diameter of 0.5–2 μm. PDA-coated s-ZnO modified with TCN (s-ZnO/PDA@TCN) exhibited small particles (beads-on-a-string) on the surface of s-ZnO, whereas s-ZnO/PDA@DOX exhibited a granular surface, as observed by FE-SEM. The average particle size of s-ZnO and TCN in s-ZnO/PDA@TCN was calculated to be 1.67 ± 0.61 μm and 6.38 ± 0.83 nm (Figure 1d,e), respectively. SEM-EDS spectra were recorded to calculate

the elemental percentages of the synthesized r/s-ZnO particles. The elemental compositions of Zn and O in the synthesized s-ZnO were 77.80 and 22.20 wt %, respectively (Figure S3(a)). Similarly, the weight percentages of Zn and O were 79.17% and 20.83% in r-ZnO, respectively. Furthermore, the s-ZnO/PDA@TCN sample exhibited average weight percentages of 30.08% Zn, 15.21% O, and 51.48% C (Figure S3(b)). In contrast, the r-ZnO/PDA@TCN sample showed weight percentages of 38.93% (Zn), 16.22% (O), and 40.71% (C) (Figure S3(c)). The increased Zn wt % and decreased carbon wt % in r-ZnO indicate a lower TCN loading compared to s-ZnO. These findings suggest that s-ZnO nanoparticles exhibit a higher drug-loading capacity. EDS of s-ZnO/PDA@DOX is provided in

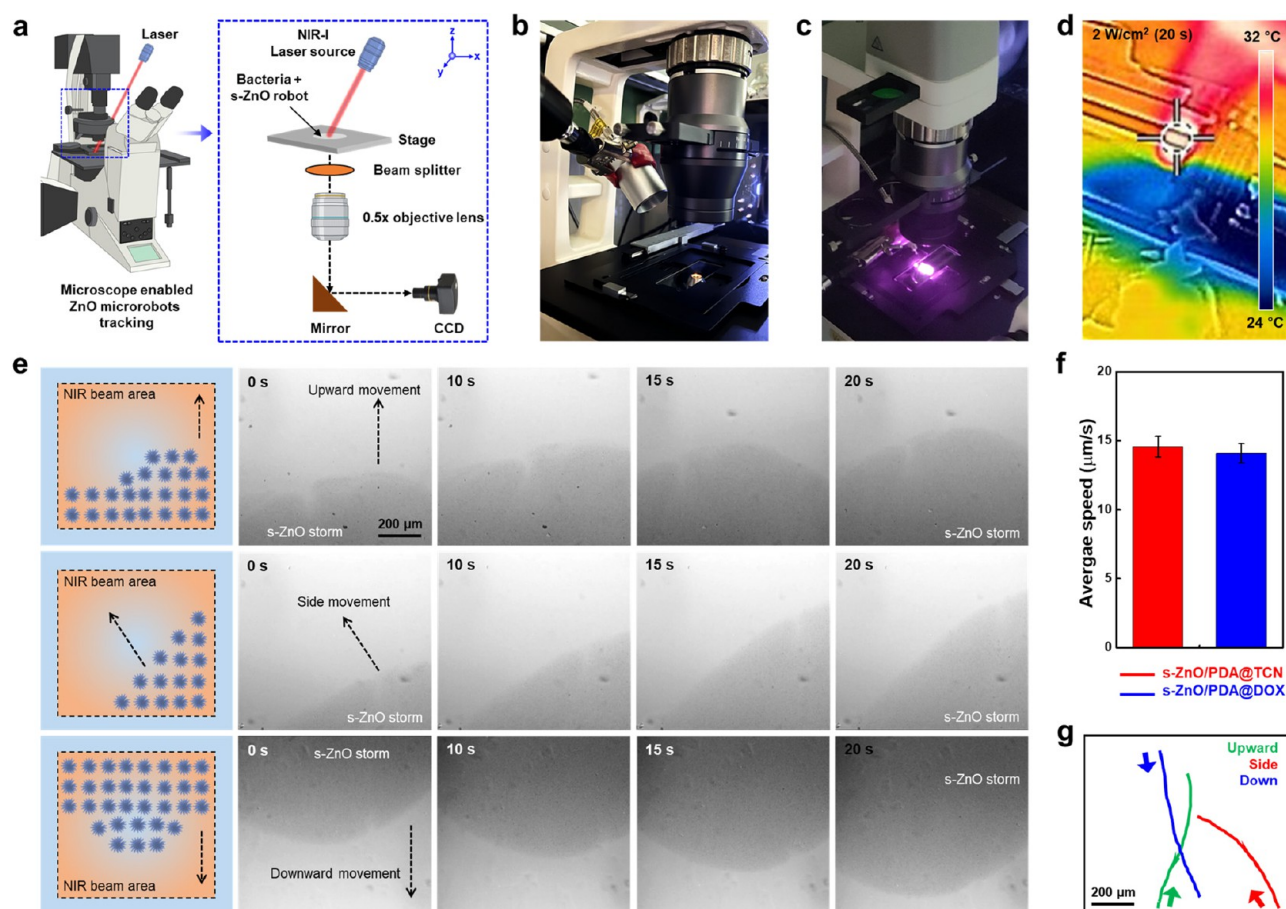


**Figure 4.** (a) Schematic illustration of the experimental setup of light-triggered microscopic platform and visualization of the *s*-ZnO nanorobots. (b, c) Digital photographs of the experimental setup and demonstration of the NIR light irradiation. (d) NIR thermal images of the platform showing the change in temperature under 808 nm NIR light (2.0 W/cm<sup>2</sup>, 20s) irradiation. (e) Microscopic images showing the motion trajectories of the *s*-ZnO nanorobots storm at indicated time points. Scale bar: 200 μm. (f) The average speed (μm/s) of the *s*-ZnO nanorobots under 808 nm NIR irradiation. (g) The movement of the *s*-ZnO nanorobots under various directions.

Figure S3(D). Consequently, further research was conducted using *s*-ZnO and *s*-ZnO/PDA@drug nanobots.

Next, we performed X-ray diffraction (XRD) to understand the structural changes in pure *s*-ZnO and its nanocomposites. As shown in Figure 2a, the *s*-ZnO particles displayed several diffraction peaks at  $2\theta = 31.92^\circ, 34.57^\circ, 36.4^\circ, 47.74^\circ, 56.7^\circ, 62.98^\circ, 66.52^\circ, 68.10^\circ, 69.23^\circ, 72.66^\circ, \text{ and } 77.12^\circ$  corresponding to the (100), (002), (101), (102), and (110), (103), (200), (112), (201), (004), and (202) planes, which resemble the standard JCPDS ID: 89-1397, indicating the formation of crystalline ZnO with unique hexagonal (wurtzite) crystals.<sup>30</sup> Interestingly, the grain size for the major diffraction peak at  $2\theta = 36.4^\circ$  of the *s*-ZnO nanospikes was calculated to be 48 nm, which was in accordance with the FE-SEM data. Furthermore, when bulk *s*-ZnO was modified with PDA and drugs, the intensity of the (101) peak decreased slightly (Figure 2b). This is due to the reduced crystallinity index (CI) of the bulk *s*-ZnO particles. The CI for pure *s*-ZnO, *s*-ZnO/PDA@TCN, and *s*-ZnO/PDA@DOX were calculated to be ~51.48%, 49.27%, and 49.66%, respectively.

The chemical alterations of bulk *s*-ZnO and its nanocomposites were recorded by using Fourier-transform infrared (FT-IR) spectroscopy, and the results are shown in Figure 2c. The absorption peak at 477.5 cm<sup>-1</sup> in bulk *s*-ZnO was attributed to the metal oxide (Zn–O) stretching vibrations, indicating the formation of zinc oxides.<sup>31,32</sup> Moreover, the peaks at 835 and

3223 cm<sup>-1</sup> was attributed to the –OH stretching and bending vibrations, respectively. Several other peaks within the 1000–1500 cm<sup>-1</sup> range indicated the presence of Zn(OH)<sub>4</sub><sup>2-</sup> and –OH mixed vibrations.<sup>32</sup> Besides, *s*-ZnO/PDA@TCN and *s*-ZnO/PDA@DOX exhibited similar absorption peaks at 474.6 and 477.1 cm<sup>-1</sup>, respectively, indicating no structural changes in the *s*-ZnO nanostructure. The peaks located at 1486 cm<sup>-1</sup> were ascribed to the aromatic C–H stretching vibration in ZnO/PDA@TCN and *s*-ZnO/PDA@DOX and were absent in bulk *s*-ZnO.<sup>33</sup> Furthermore, the absorption peaks at approximately 1590 and 1576 cm<sup>-1</sup> were attributed to the C=N stretching vibrations of PDA in ZnO/PDA@TCN and *s*-ZnO/PDA@DOX. Notably, the peak at around 1303 cm<sup>-1</sup> was associated with the C–O stretching and bending vibrations of TCN, indicating the successful binding of TCN onto the *s*-ZnO/PDA surface.<sup>34</sup> The FT-IR spectra of the *s*-ZnO/PDA@DOX exhibited an absorption peak at around 1617 cm<sup>-1</sup> corresponding to the carbonyl (C=O) stretching of the anthracene ring of DOX, absent in *s*-ZnO, meaning that the *s*-ZnO particles interact with the quinone oxygen of the DOX molecule through chemical adsorption.<sup>35</sup> The peak located at 1413 cm<sup>-1</sup> in *s*-ZnO/PDA@DOX indicates the presence of the aromatic C–H stretching vibration of the DOX molecule. Our results indicate the formation of highly crystalline ZnO nano spikes that were successfully modified with PDA, TCN, and DOX for therapeutic applications.

**Table 1. Comparative Study of Various Micro/Nanobots as Photosensitizers for Antibacterial Therapy<sup>a</sup>**

micro/nanobots	size	power source	microorganism	mechanism	refs
star-shaped BiVO <sub>4</sub> micromotors	4–8 μm	visible light	<i>Saccharomyces cerevisiae</i>	photocatalytic generation of ROS, disruption of cell membrane	40
ZnO/Ag micromotors	~5 μm	UV light	<i>Staphylococcus aureus</i> , <i>Pseudomonas aeruginosa</i>	mechanical disruption due to ROS generation	41
MXene-sAuNR nanorobot	N/A	sunlight, NIR light (808 nm)	<i>Escherichia coli</i> , <i>Staphylococcus aureus</i>	knife function MXene edge	42
MUCR@MLMD@LAA	N/A	magnetic field	<i>Enterococcus faecalis</i> , <i>Escherichia coli</i>	chemotaxis agent attracts more bacteria and kill	43
PNM-MN	~80 nm	NIR light (808 nm)	<i>Candida albicans</i>	photothermal effect	44
HSMV nanoswimmer	100–500 nm	NIR light (650 nm)	<i>Staphylococcus aureus</i>	killing of bacteria by membrane disruption	45
s-ZnO/PDA/TCN nanobots	85–100 nm core with spikes of 1.6 nm	NIR light (808 nm)	<i>Escherichia coli</i> <i>Staphylococcus epidermidis</i>	TCN delivery and photothermal killing of bacteria	this study

<sup>a</sup>BiVO<sub>4</sub>: bismuth vanadate; ZnO: zinc oxide; Ag: silver; sAuNR: small gold nanorods; MUCR@MLMD@LAA: magnetic urchin-like capsule robots loaded with magnetic liquid metal drops and L-aspartic acid; PNM-MN: parachute-like nanomotors loaded with miconazole nitrate; HSMV: gold-functionalized mesoporous silica half shell motor loaded with vancomycin.

Drug encapsulation is a major standard for the fabrication of nanocarriers. The drug encapsulation efficiencies in the s-ZnO/PDA@TCN and s-ZnO/PDA@DOX composites were determined by measuring the intensity of the UV–vis absorption peaks. The calibration curves for TCN and DOX are given in Figure S4. The TCN and DOX encapsulation rates on s-ZnO/PDA were determined to be 12.82% and 2.8%, respectively, using the equations provided in Section 2.2. The encapsulation efficiency of DOX was low; however, TCN exhibited high encapsulation efficiencies on spiky ZnO/PDA.

**3.2. Photothermal Performance of the s-ZnO/PDA Nanobots.** Figure 3a,b shows the time-dependent temperature increase profile of the s-ZnO and s-ZnO/PDA nanobots under 1.0 and 2.0 W/cm<sup>2</sup> NIR light irradiation for 5 min (300 s). It is interesting to note that at a 0.1 mg/mL concentration the samples exhibited minor changes in temperature at 1.0 W/cm<sup>2</sup> power density. However, at 2.0 W/cm<sup>2</sup> power density, the temperature of s-ZnO was gradually raised to 43.1 °C. Besides, the nanobot suspension showed a significant temperature increase from 75.1 to 88.3 °C at a concentration of 0.5 mg/mL when the power density was increased from 1.0 to 2.0 W/cm<sup>2</sup>, respectively. The thermal images of the temperature changes are shown in Figure 3c. Therefore, the change in the photothermal properties of the fabricated nanobots was not only laser power-dependent but also concentration-dependent. Wu et al.<sup>36</sup> previously demonstrated the exceptional NIR-responsive properties of cerium-loaded ZnO/PDA composites for cancer photodynamic therapy. Consistent with these results, we anticipate that the fabricated s-ZnO/PDA-based nanobots exhibit good photothermal properties for therapeutic applications. Based on our observations, we selected a 0.5 mg/mL concentration with a laser power density of 2.0 W/cm<sup>2</sup> for the rest of the experiments.

NIR light was absorbed by a PDA coating on the s-ZnO/PDA@drug nanorobots. PDA uses photothermal action to convert photon energy into heat efficiently.<sup>37</sup> The s-ZnO/PDA of the nanorobots increased in response to NIR laser irradiation. Nanorobots can travel along temperature gradients using PDA thermophoretic force.<sup>38</sup> Thermophoresis uses temperature changes such as Brownian motion. Therapeutic payloads can be delivered to tumors or infected tissues using precisely positioned and dispersed nanorobots, which minimize off-target effects.

Radical formation in s-ZnO/PDA under NIR light illumination was investigated by using ESR tests. Figure 3d shows that

the sample exposed to NIR light initially exhibited no significant response. However, after 5 min of NIR light exposure, a distinct triple peak corresponding to PDA was observed. This triple peak, characteristic of singlet-state oxygen (<sup>1</sup>O<sub>2</sub><sup>-</sup>), was identified using a TEMP probe.<sup>39</sup> These findings suggest that s-ZnO/PDA does not produce radicals in the absence of NIR light; however, under NIR light exposure, <sup>1</sup>O<sub>2</sub> radicals are generated, indicating the potential for reactive oxygen species (ROS) generation in anticancer and antibacterial applications.

### 3.3. Study of NIR-Triggered Nanobots Movement.

Figure 4a depicts the experimental setup for NIR-triggered s-ZnO nanobot tracking and movement analysis. The system included an inverted optical microscope equipped with a closed coupled device (CCD) camera and an 808 nm NIR light source with a digital control system. The digital photographs of the experimental setup are shown in Figure 4b,c. The NIR light was arranged diagonally with regard to the sample stage, where the nanobot movement was monitored. A microscope slide with a few drops (~400 μL) of the nanobot suspension was used for the experiment. During the experiment, the NIR light with a power density of 2.0 W/cm<sup>2</sup> (laser spot diameter: 500 μm) was irradiated onto the sample surface (Figure 4d), and the heat generation was monitored subsequently (Figure S5). Upon irradiation, we tested three experimental conditions for laser light movement: (1) upward, (2) side, and (3) downward. Glass and water have respective thermal conductivities of 1.3 and 0.6 W/mK. Upon NIR laser irradiation, a temperature gradient rapidly formed at the air–water interface of the suspension, precisely centered on the area where the laser was illuminating.<sup>2</sup> It was interesting to note that the s-ZnO nanobot storm was effectively moved toward the light source when controlled in the upward, side, and downward directions within 20 s (Figure 4e). We observed no observable differences in the speeds of the TCN- and DOX-loaded nanobot samples. The average speed of s-ZnO/PDA@TCN and s-ZnO/PDA@DOX was calculated to be 14.57 and 13.99 μm/s, respectively (Figure 4f). Based on the microscopic movement and video data, the movement trajectories of the nanobots are shown in Figure 4g. The movement speed reported in this study was quite good compared to that in a recent study by Song et al.,<sup>2</sup> in which PDA-coated carbonized sunflower sporopollenin (SPG) microbots were used for bacterial capture and clearance.

In this study, the movement of nanobots was primarily facilitated by the incorporation of PDA, which imparts light-sensitive properties to the nanobots. Absorbance spectra of s-

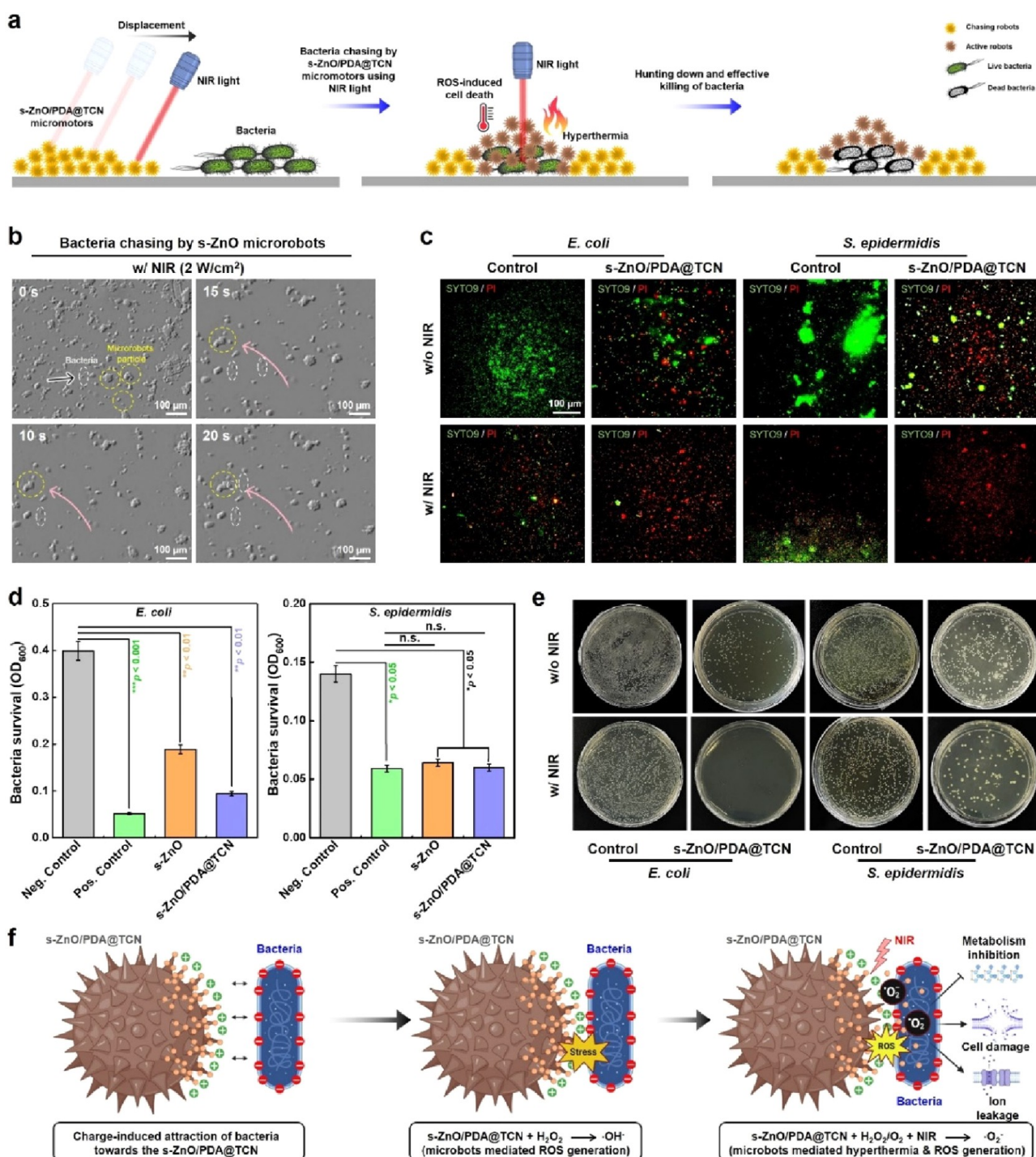


**Figure 5.** (a) Schematic illustration of the chasing mechanism by the s-ZnO/PDA/TCN nanorobots and photothermal killing of bacterial pathogen. (b) Bright field images of the gathered nanorobots (dotted yellow circle) toward bacteria (dotted white circle) at indicated time points. Scale bar: 100 μm. (c) Representative SYTO9 (live) and PI (dead) staining of the *E. coli* and *S. epidermidis* w/ or w/o NIR irradiation. Scale bar: 100 μm. (d) Test of bacterial survivability in terms of optical density (OD<sub>600</sub>) after 6 h of incubation with s-ZnO and s-ZnO/PDA@TCN (Pos. control: pure tetracycline 1 mg/mL). Data reported as mean ± O.D. of triplicated (n = 3) experiments, statistical significance at \*p < 0.05 and \*\*p < 0.01. (e) Representative agar plate assay showing the antibacterial performance of the fabricated nanobots w/ or w/o NIR light irradiation after 6 h of incubation. (f) Schematic illustration of the antibacterial mechanisms of the NIR-responsive s-ZnO/PDA@TCN nanobots.

ZnO and s-ZnO/PDA is shown in Figure S6. When exposed to light, light absorbing PDA undergoes photochemical reactions or structural changes, converting light energy into heat through a photothermal process. This leads to the generation of temperature gradients in the surrounding environment through localized heating. The PDA-coated nanorobots then move along

these thermal gradients, propelled by thermophoretic forces. Leveraging these controlled movements, nanorobots can be precisely dispersed within biological tissues or targeted areas to deliver therapeutic drugs to tumors or infected tissues with minimal off-target effects. Our results demonstrate that the fabricated s-ZnO-based nanobots can be efficiently gathered

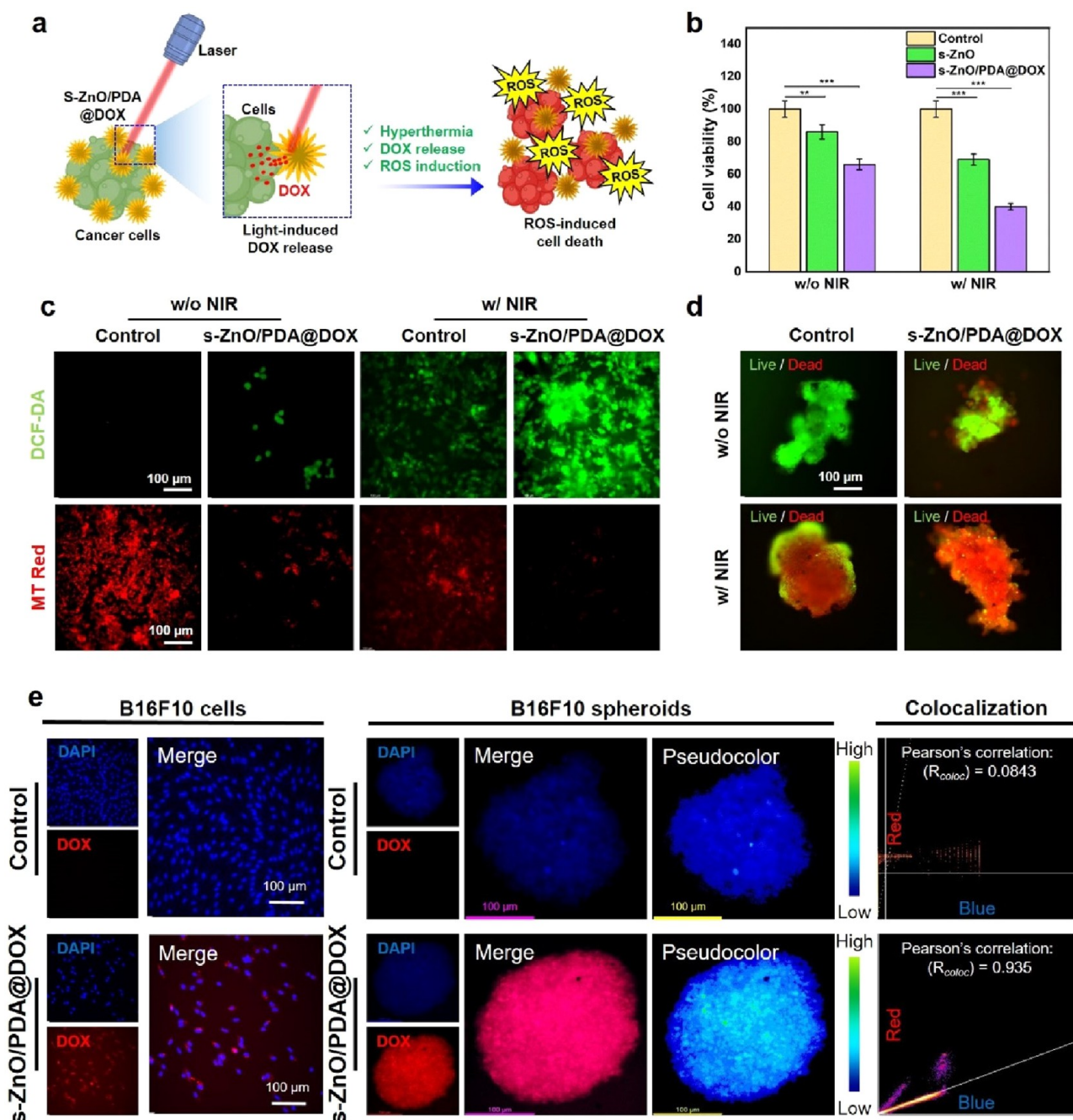


**Figure 6.** (a) Schematic illustration of NIR-triggered DOX release and hyperthermia-induced cell death of cancer cells. (b) WST-8 assay of B16F10 melanoma cells in the presence of s-ZnO and s-ZnO/PDA/DOX after 24 h of incubation. Data reported as percentage of triplicated ( $n = 3$ ) experiments, statistical significance at  $*p < 0.05$  and  $***p < 0.001$ . (c) Representative DCF-DA and MT Red staining of B16F10 cells showing the intracellular ROS and mitochondria damage w/ or w/o NIR irradiation. Scale bar: 100  $\mu\text{m}$ . (d) FL microscopy images showing the live/dead staining of B16F10 spheroids w/ or w/o NIR irradiation. Scale bar: 100  $\mu\text{m}$ . (e) s-ZnO/PDA@DOX encapsulation in B16F10 cells and spheroids. The nanobots uptake and DOX accumulation was quantified through Pearson's colocalization test ( $R_{coloc}$ ). Scale bar: 100  $\mu\text{m}$ .

using NIR light and can be used as ideal nanoplatforms for therapeutics. A comparative study of the applications and performances of various pollen-derived and pollen-inspired micro/nanobots is presented in Table 1.

**3.4. Antibacterial Performance of the Nanobots.** NIR light possesses unparalleled benefits, including profound tissue penetration and low harm to biological cells caused by light exposure.<sup>46</sup> Bactericidal effects of nanobots were investigated after assessment of the phototaxis and motion behavior of the microbots in the presence of NIR light. The effectiveness of s-

ZnO/PDA@TCN nanobots as bactericidal agents was evaluated using two types of bacteria, *E. coli* and *S. epidermidis*, as representative Gram-positive and Gram-negative bacteria, respectively. ZnO NPs have been shown to exhibit antibacterial properties.<sup>47</sup> However, the effectiveness of this combination with NIR irradiation remains unknown.

To demonstrate the benefits of s-ZnO/PDA@TCN in the presence and absence of NIR light, we conducted *in vitro* antibacterial experiments by placing s-ZnO/PDA@TCN nanobots in the presence of adsorbate and allowing bacteria to grow

alongside them. Antibacterial activity was evaluated using the live/dead assay and agar diffusion method. Figure 5a shows a schematic representation of the process of applying nanobots for bacterial eradication, followed by exposure to NIR light. As previously mentioned, when exposed to NIR light, the s-ZnO/PDA@TCN nanobots demonstrated successful mobility (Figure 5b). The sample was incubated with bacteria for 6 h to assess the bactericidal efficacy. The optical density (Figure 5d) of the bacteria exhibited a statistically significant decrease compared with that of the control. The impact of nanobots lacking NIR was highly favorable for *E. coli*. Nevertheless, the bactericidal effect was less pronounced in Gram-positive than in Gram-negative bacteria. The bacteria were eradicated by NIR irradiation, indicating the efficacy of the sample against Gram-positive bacteria. However, it was necessary to extend the duration of the exposure.

Following exposure to 808 nm NIR light for 5 min (2.0 W/cm<sup>2</sup>), the s-ZnO/PDA@TCN nanobots were subjected to a live/dead experiment using SYTO9 and propidium iodide to assess their antibacterial effectiveness. SYTO9 is recognized for its ability to color all cells green uniformly, but propidium iodide can enter compromised bacterial membranes and displace the green fluorescence with red. Therefore, the antibacterial action was documented by distinguishing between the green and red patches on the surface. Figure 5c shows the fluorescence microscopic images of *E. coli* and *S. epidermidis* in the presence of nanobots with and without irradiation by NIR light. Green fluorescence was observed in the control group exposed to NIR light. However, red fluorescence was observed when NIR light was used in the control group, indicating that NIR light has limited bactericidal capabilities. In contrast, the nanobot sample exhibited a higher intensity of red fluorescence and a lower intensity of green fluorescence when exposed to NIR light. In the s-ZnO/PDA@TCN nanobot group exposed to NIR light, the bacteria exhibited the most pronounced red fluorescence, indicating that the nanobots effectively eradicated bacteria when subjected to NIR light. However, the sample of *S. epidermidis* did not demonstrate any significant efficacy.

The agar plate results depicted in Figure 5e for *E. coli* and *S. epidermidis* were consistent with the live/dead results. The nanobots exhibited significant antibacterial efficacy against *E. coli* in the presence and absence of NIR light. Compared with the control set, the bactericidal effect against *S. epidermidis* was notably significant. The antibacterial efficacy of s-ZnO/PDA@TCN against *E. coli* and *S. epidermidis* can be explained by the redox transfer and photothermal heat-shock mechanisms. The polycatechol groups of PDA which was attached to the s-ZnO reacted with free oxygen to produce hydrogen peroxide (H<sub>2</sub>O<sub>2</sub>) via electron transfer and induced the formation of hydroxyl radicals ( $\cdot\text{OH}^-$ ), which was captured by the bacteria. Following that, the radicals inhibit the metabolism and damage the cell membrane, resulting in mass ion leakage. Besides, the presence of NIR enhanced the killing effect by inducing the local hyperthermia and facilitated the TCN release from the s-ZnO/PDA. Thus, hyperthermia with TCN synergistically induced the membrane damage and promoted the formation of singlet-oxygen ( $\cdot\text{O}_2^-$ ) inside the *E. coli* and *S. epidermidis*, which ultimately triggered the ability to lose the biological activity. Figure 5f schematically demonstrates the antibacterial mechanisms of the s-ZnO/PDA@TCN nanobots.

**3.5. Anticancer Activities of the Nanobots.** Stimuli-responsive nanomaterials or nanosensitizers have long been known to have enhanced anticancer/antitumor properties

owing to the local hyperthermia or induction of reactive oxygen species (ROS).<sup>48,49</sup> For instance, zinc-based nanostructures, such as ZnO has been reported to have outstanding anticancer property due to the induction of ROS, inhibition of protein synthesis, and induction of apoptosis in cancer cells.<sup>50–53</sup> Recently, various stimuli-responsive micro/nanorobots have been shown as a promising alternative for tumor therapy owing to the nanoinvasive monitoring and circulating nature through the blood vessels.<sup>1</sup> Herein, we reported the use of s-ZnO/PDA@DOX-based photosensitizer for NIR light-triggered DOX delivery, hyperthermia, ROS production, and the subsequent killing of B16F10 melanoma cells. A schematic illustration of NIR-triggered anticancer therapy is shown in Figure 6a. HDF, B16F10 cells, and spheroids were incubated with s-ZnO and s-ZnO/PDA@DOX, and their viability was assessed by using the WST-8 assay. Figure 6b displays slight toxicity in the B16F10 cells w/ and w/o NIR irradiation in the presence of s-ZnO than control. However, the s-ZnO/PDA@DOX-treated group exhibited potential toxicity ( $***p < 0.001$ ) after 24 h of incubation without NIR irradiation. In addition, upon NIR irradiation, s-ZnO/PDA@DOX exhibited higher cytotoxicity (~60.32%;  $***p < 0.001$ ) in B16F10 cells (Figure 6b), suggesting their therapeutic efficacy. Additionally, we investigated the s-ZnO/PDA effect w/ and w/o NIR on HDF to check the cytotoxicity and NIR influence on the surrounding cells (Figure S7). s-ZnO and s-ZnO/PDA@DOX exhibited low toxicity in HDF, indicating the tolerance to NIR light and the biocompatibility of the nanobots. Peng et al.<sup>54</sup> reported the use of light-triggered and self-propelled hematite microrobots for GSH-depleted tumor therapy. In another study, a dual-powered *Magnetospirillum magneticum* (AMB-1)-based biomagnetobot was used for triggering anticancer property via inducing the NIR hyperthermia and ROS.<sup>16</sup> Consistent with this report, our fabricated s-ZnO/PDA@DOX nanobots exhibited superior melanoma cell killing efficacy under 808 nm NIR light, making it an effective photosensitizer.

To evaluate the mechanism of cell death, we performed DCF-DA staining, MitoTracker (MT) Red staining, and apoptosis analysis. As shown in Figure 6c, the B16F10 cells exhibited a small amount of intracellular ROS and few mitochondrial clusters without NIR irradiation in the presence of s-ZnO/PDA@DOX. However, after NIR irradiation for 5 min, elevated amounts of ROS were detected in the s-ZnO/PDA@DOX-treated groups, suggesting the release of both DOX and ROS. This was also reflected in the destruction of the mitochondrial clusters. The NIR-treated group displayed fewer mitochondrial clusters than did the untreated group. To confirm the NIR-induced ROS and cell death, we evaluated the cytotoxicity of B16F10 spheroids by live and dead staining with s-ZnO/PDA@DOX and NIR light. The results are presented in Figure 6d. Interestingly, the spheroid size and number of dead cells gradually increased after s-ZnO/PDA@DOX and NIR light treatments, suggesting that the nanobots can be used to kill solid tumors.

The role of fabricated nanobots in apoptosis induction was also evaluated using PI/Annexin-V staining with or without NIR irradiation, and the results are shown in Figure S8. Notably, the groups that received no NIR and no samples displayed 0.0% apoptotic cells during cytometry. However, the groups with no NIR but s-ZnO/PDA@DOX exhibited 7.9% apoptotic cells, meaning that the toxicity of s-ZnO and DOX triggered the apoptosis. Interestingly, the groups with NIR and s-ZnO/PDA@DOX also exhibited a slightly higher amount of apoptotic

Table 2. Comparative Study of Various Micro/Nanobots as Photosensitizers for Anticancer Therapy<sup>a</sup>

micro/nanorobot	size	power source	cell lines	mechanism	refs
(Pd@Au)/Fe <sub>3</sub> O <sub>4</sub> @Sp-DOX microrobots	~200 μm in length	NIR light (808 nm)	769-P and EC109 cancer cells	chemo-photothermal therapy, drug delivery	56
nanomotors (PTX-loaded CaCO <sub>3</sub> -PDA-PEI-CAT-FA-siRNA) hydrogel	60.0 ± 5.0 nm	endogenous H <sub>2</sub> O <sub>2</sub> , acidic environment	4T1 cells, L929 cells	destruction of tubulin in cancer cells	57
sunflower pollen grain (SPG)-based magnetic urchin-like microswimmers	20–30 μm	magnetic field	HeLa cells	DOX-based killing, cell drilling	58
pine pollen-based micromotors	30–40 μm	magnetic field	HeLa cells	DOX therapy	59
neutrophil-based microbots	~10 μm	magnetic field, NIR light	bEnd.3 cells, G422 cells	targeted penetration and paclitaxel delivery	60
ECM-mimicking microbots	30–500 μm	magnetic field	MDA-MB-231 cells	specific capture, inhibit cell metastasis	61
DOX@SFPμP-BioBots	~30 μm	magnetic field	A2780 cells	DOX release and therapy	55
s-ZnO/PDA/DOX nanobots	85–100 nm core with spikes of 1.6 nm	NIR light (808 nm)	B16F10 cells and spheroids	DOX release, photothermal therapy, and ROS amplification	this study

<sup>a</sup>(Pd@Au)/Fe<sub>3</sub>O<sub>4</sub>@Sp-DOX: doxorubicin-loaded palladium–gold nanoparticles of *Spirulina* biotemplate with iron oxide deposition; PTX: paclitaxel; CaCO<sub>3</sub>: calcium carbonate; PDA: polydopamine; PEI: polyethylenimine; CAT: catalase; FA: folic acid; siRNA: small interfering RNA; H<sub>2</sub>O<sub>2</sub>: hydrogen peroxide.

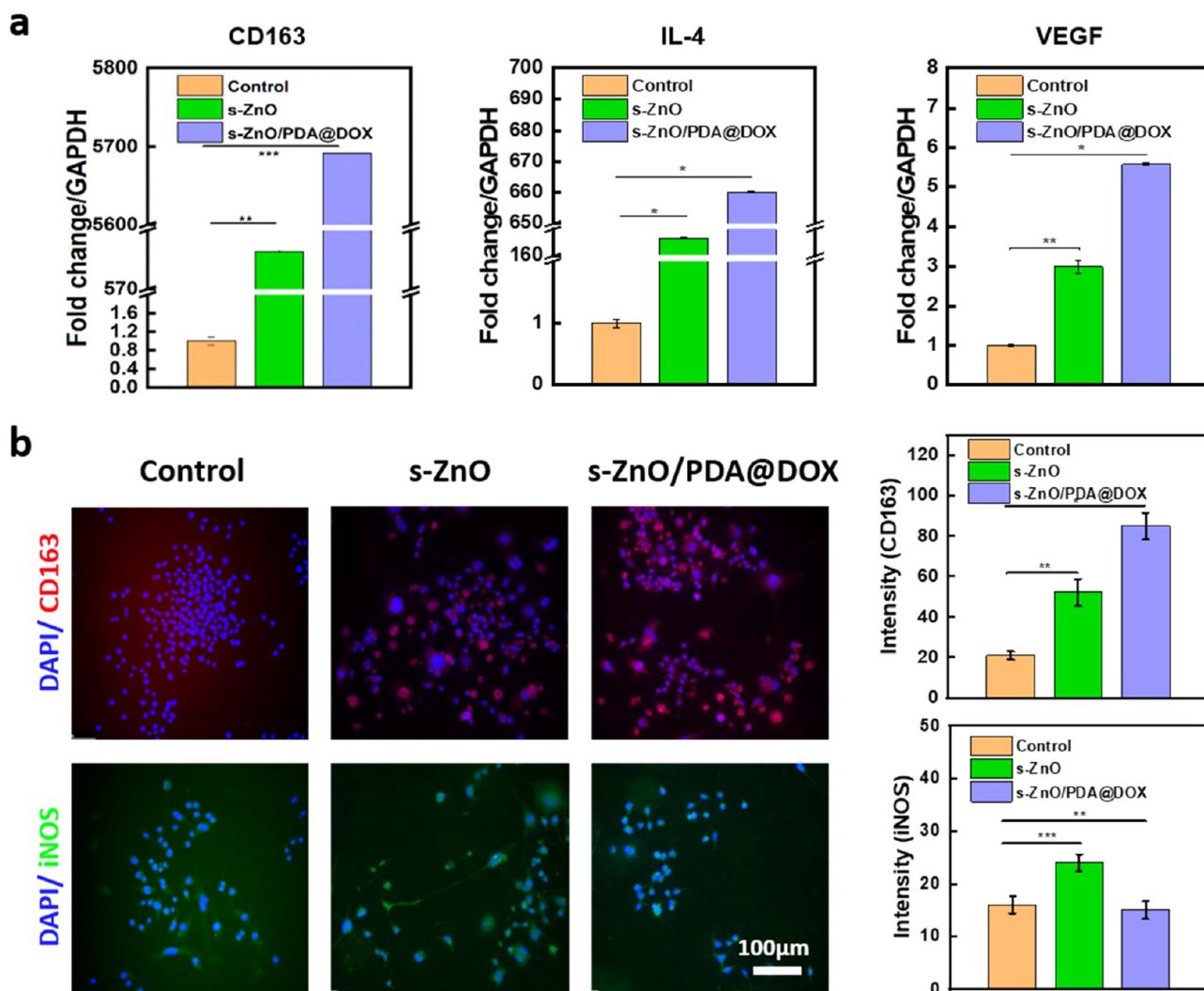


**Figure 7.** Immunogenic properties of the fabricated nanobots *in vitro*. (a) qRT-PCR results showing the mRNA expression of various inflammatory genes (CD163, IL-4, and VEGF) in RAW 264.7 cells after 24 h of incubation. (b) Representative fluorescence micrographs of the RAW 264.7 cells showing the intracellular expression of M1 macrophage maker (iNOS) and M2 polarization marker (CD163). Scale bar: 100 μm. Data reported as mean ± s.d. of triplicated ( $n = 3$ ) experiments, statistical significance at  $*p < 0.05$ ,  $**p < 0.01$ , and  $***p < 0.001$  (one-way ANOVA test).

cells (11.7%), suggesting that NIR irradiation at a power density of 2.0 W/cm<sup>2</sup> induced hyperthermia and triggered DOX release

and synergistic cell death. The quantification of the apoptosis study is given in Figure S8. Mayorga-Martinez et al.<sup>55</sup> recently

reported a similar kind of biobot using gold and cobalt codoped sunflower pollen for fast release of DOX and attract the tumor cells under 3 mT (0.3 Hz) magnetic fields. This reported that the average viability of the A2780 cells was around 36.9%, much higher than that in our present study (~16.32%). Therefore, the sunflower-inspired metal-based spiky nanobots are intelligent, exhibit superior photothermal properties, and could be an ideal nanotherapeutic platform for treating metastatic cancers.

s-ZnO/PDA@DOX encapsulation within the B16F10 cells and spheroids was also studied. As depicted in Figure 6e, the red fluorescence intensity of DOX-loaded nanoparticles within the cells following a 24 h incubation period signified the successful internalization of the synthesized nanoparticles by both B16F10 cells and spheroids. In contrast, the control group exhibited negligible fluorescence, which was attributed to the lack of s-ZnO/PDA@DOX nanobots. Notably, the spheroids displayed a pronounced red fluorescence, indicating the presence of nanobots. Furthermore, the intensity-based pseudocolor image and subcellular colocalization test revealed a high coefficient value for the s-ZnO/PDA@DOX-treated group ( $R_{\text{coloc}} = 0.935$ ) than the control ( $R_{\text{coloc}} = 0.0843$ ), suggesting the greater accumulation of DOX-loaded nanobots in B16F10 spheroids. These findings support the efficient uptake of nanobots, which enhances the targeting capabilities of nanodrug delivery platforms. A comparative study of various stimuli-regulated micro/nanobots for cancer drug delivery and photothermal therapy is presented in Table 2.

**3.6. Immunogenic Properties of s-ZnO/PDA@DOX.** It is well established that macrophages displayed pro-inflammatory activation in response to the foreign particles.<sup>62,63</sup> Thus, the activation of the M1 phenotype triggers site-specific inflammation, resulting in the activation/inactivation of the test material.<sup>64</sup> This study aimed to investigate whether s-ZnO/PDA@DOX nanobots induce M2 polarization in macrophages, suggesting that they have limited foreign body response. The qRT-PCR analysis assessed the M2 gene expression in the presence of s-ZnO/PDA@DOX nanobots. Remarkably, as shown in Figure 7a, treatment with nanobots resulted in the upregulation of CD163 (>100-fold, \*\*\* $p < 0.001$ ), IL-4 (>100-fold, \* $p < 0.05$ ), and VEGF (>5-fold, \* $p < 0.05$ ) genes, indicative of M2 polarization in macrophages. These findings suggest that s-ZnO/PDA@DOX treatment promotes M2 polarization, implying that the nanobots do not provoke serious immune response. Furthermore, the elevated subcellular localization of CD163 and less accumulation of iNOS confirm the secretion of anti-inflammatory cytokines (Figure 7b), underscoring the excellent biocompatibility of our nanobots and their ability to avoid triggering an immune response in the cellular microenvironment.

## 4. CONCLUSION

In this study, sunflower pollen-inspired spiky zinc nanobots were fabricated for targeted antibacterial and anticancer therapies. A multimodal therapeutic delivery platform was created by integrating photoresponsive characteristics and medication loading into the nanobots. The characterization of the nanobots revealed their unique morphology, crystal structure, and chemical composition, laying the foundation for many applications. The nanobots exhibited promising photothermal performance under NIR light, suggesting regulated hyperthermia. We also studied their NIR-triggered mobility, showing that nanobots can travel efficiently in response to 808 nm NIR laser light with an average speed of ~14.57 and ~13.99  $\mu\text{m/s}$  at

2.0 W/cm<sup>2</sup> power density. This mobility enables targeted antibacterial therapies to kill *E. coli* and *S. epidermidis*. In addition to their antibacterial use, nanobots have shown significant performance as photosensitizers for cancer treatment, allowing targeted killing and inducing DOX delivery. They photoinduced cytotoxicity in B16F10 melanoma cells, demonstrating their nanotherapeutic potential. NIR light enhances ROS amplification, mitochondrial disruption, and apoptosis. The sunflower pollen-inspired s-ZnO/PDA@Drug motility, photothermal capabilities, and drug delivery ability with less foreign body response may be useful for targeted antibacterial and anticancer therapies for chronic infections and malignancies. This study advances nanomedicine by providing a versatile platform for precise and effective therapeutic treatment. Further research and optimization of these nanobots could lead to biomedical applications.

## ■ ASSOCIATED CONTENT

### Supporting Information

The Supporting Information is available free of charge at <https://pubs.acs.org/doi/10.1021/acsabm.4c00092>.

FE-SEM morphology of sunflower pollen; FE-SEM images of round and spiky ZnO nanobots; EDS elemental mapping images of the various nanobots; TCN and OX calibration curve; NIR thermal images of the nanobots; UV-vis absorption spectra of s-ZnO and s-ZnO/PDA nanobots; cytotoxicity profile of nanobots on HDFs; FACS analysis of B16F10 cells w/ or w/o NIR irradiation (PDF)

## ■ AUTHOR INFORMATION

### Corresponding Author

**Ki-Taek Lim** – Department of Biosystems Engineering, Kangwon National University, Chuncheon 24341 Gangwon-do, Republic of Korea; Institute of Forest Science, Kangwon National University, Chuncheon 24341 Gangwon-do, Republic of Korea; Interdisciplinary Program in Smart Agriculture, Kangwon National University, Chuncheon 24341 Gangwon-do, Republic of Korea; [orcid.org/0000-0003-2091-788X](https://orcid.org/0000-0003-2091-788X); Email: [ktlim@kangwon.ac.kr](mailto:ktlim@kangwon.ac.kr)

### Authors

**Sayan Deb Dutta** – Department of Biosystems Engineering, Kangwon National University, Chuncheon 24341 Gangwon-do, Republic of Korea; Institute of Forest Science, Kangwon National University, Chuncheon 24341 Gangwon-do, Republic of Korea; Center for Surgical Bioengineering, School of Medicine, University of California Davis, Davis, California 95817, United States

**Rachmi Luthfikasari** – Department of Biosystems Engineering, Kangwon National University, Chuncheon 24341 Gangwon-do, Republic of Korea

**Tejal V. Patil** – Department of Biosystems Engineering, Kangwon National University, Chuncheon 24341 Gangwon-do, Republic of Korea; Interdisciplinary Program in Smart Agriculture, Kangwon National University, Chuncheon 24341 Gangwon-do, Republic of Korea

**Keya Ganguly** – Department of Biosystems Engineering, Kangwon National University, Chuncheon 24341 Gangwon-do, Republic of Korea; Institute of Forest Science, Kangwon National University, Chuncheon 24341 Gangwon-do, Republic of Korea

**Youjin Seol** – Department of Biosystems Engineering, Kangwon National University, Chuncheon 24341 Gangwon-do, Republic of Korea

**Aayushi Randhawa** – Department of Biosystems Engineering, Kangwon National University, Chuncheon 24341 Gangwon-do, Republic of Korea; Interdisciplinary Program in Smart Agriculture, Kangwon National University, Chuncheon 24341 Gangwon-do, Republic of Korea

Complete contact information is available at:  
<https://pubs.acs.org/10.1021/acsabm.4c00092>

### Author Contributions

<sup>#</sup>S.D.D., R.L., and T.V.P. contributed equally to this manuscript. S.D.D.: Conceptualization, Methodology, Formal Analysis, Software, Visualization, Project administration, Writing—original draft, Writing—review and editing; R.L.: Conceptualization, Methodology, Formal Analysis, Writing—original draft, Writing—review and editing; T.V.P.: Methodology, Formal Analysis, Visualization, Writing—original draft, Writing—review and editing; K.G., Y.S., and A.R.: Formal analysis; Methodology; Visualization; K.T.L.: Supervision; Project Administration; Writing—review and editing, Funding acquisition.

### Notes

The authors declare no competing financial interest.

### ACKNOWLEDGMENTS

This study was supported by the Basic Science Research Program through the National Research Foundation of Korea funded by the Ministry of Education (NRF-2018R1A16A1A03025582; NRF2022R1I1A3063302). This work was supported by the Innovative Human Resource Development for Local Intellectualization Program through the Institute of Information and Communications Technology Planning and Evaluation (IITP) Grant funded by the Korea government (MSIT; IITP-2024-RS-2023-00260267).

### REFERENCES

- (1) Schmidt, C. K.; Medina-Sánchez, M.; Edmondson, R. J.; Schmidt, O. G. Engineering microrobots for targeted cancer therapies from a medical perspective. *Nat. Commun.* **2020**, *11* (1), 5618.
- (2) Song, L.; Zhang, S.; Wang, Q.; Chen, W.; Liu, B.; Zhao, Y.-D. Light-controlled microrobots gathering as a sterilization platform for highly efficient capturing, concentrating and killing targeted bacteria. *Chemical Engineering Journal* **2022**, *435*, 135067.
- (3) Dekanovsky, L.; Ying, Y.; Zelenka, J.; Plutnar, J.; Beladi-Mousavi, S. M.; Křížová, I.; Novotný, F.; Ruml, T.; Pumera, M. Fully Programmable Collective Behavior of Light-Powered Chemical Microrobots: pH-Dependent Motion Behavior Switch and Controlled Cancer Cell Destruction. *Adv. Funct. Mater.* **2022**, *32* (38), 2205062.
- (4) Fan, D.; Yin, Z.; Cheong, R.; Zhu, F. Q.; Cammarata, R. C.; Chien, C.; Levchenko, A. Subcellular-resolution delivery of a cytokine through precisely manipulated nanowires. *Nature Nanotechnol.* **2010**, *5* (7), 545–551.
- (5) Kim, K.; Xu, X.; Guo, J.; Fan, D. Ultrahigh-speed rotating nanoelectromechanical system devices assembled from nanoscale building blocks. *Nat. Commun.* **2014**, *5* (1), 3632.
- (6) Han, K.; Shields IV, C. W.; Velev, O. D. Engineering of self-propelling microrobots and microdevices powered by magnetic and electric fields. *Adv. Funct. Mater.* **2018**, *28* (25), 1705953.
- (7) Park, J.; Jin, C.; Lee, S.; Kim, J. Y.; Choi, H. Magnetically actuated degradable microrobots for actively controlled drug release and hyperthermia therapy. *Adv. Healthcare Mater.* **2019**, *8* (16), 1900213.
- (8) Nguyen, V. D.; Min, H.-K.; Kim, H. Y.; Han, J.; Choi, Y. H.; Kim, C.-S.; Park, J.-O.; Choi, E. Primary macrophage-based microrobots: an

effective tumor therapy in vivo by dual-targeting function and near-infrared-triggered drug release. *ACS Nano* **2021**, *15* (5), 8492–8506.

(9) Park, J.; Kim, J. Y.; Pane, S.; Nelson, B. J.; Choi, H. Acoustically mediated controlled drug release and targeted therapy with degradable 3D porous magnetic microrobots. *Adv. Healthcare Mater.* **2021**, *10* (2), 2001096.

(10) Del Campo Fonseca, A.; Glück, C.; Droux, J.; Ferry, Y.; Frei, C.; Wegener, S.; Weber, B.; El Amki, M.; Ahmed, D. Ultrasound trapping and navigation of microrobots in the mouse brain vasculature. *Nat. Commun.* **2023**, *14* (1), 5889.

(11) Li, J.; Mayorga-Martinez, C. C.; Ohl, C. D.; Pumera, M. Ultrasonically Propelled Micro-and Nanorobots. *Adv. Funct. Mater.* **2022**, *32* (5), 2102265.

(12) Palagi, S.; Mark, A. G.; Reigh, S. Y.; Melde, K.; Qiu, T.; Zeng, H.; Parmeggiani, C.; Martella, D.; Sanchez-Castillo, A.; Kapernaum, N.; et al. Structured light enables biomimetic swimming and versatile locomotion of photoresponsive soft microrobots. *Nature Materials* **2016**, *15* (6), 647–653.

(13) Bunea, A. I.; Martella, D.; Nocentini, S.; Parmeggiani, C.; Taboryski, R.; Wiersma, D. S. Light-powered microrobots: challenges and opportunities for hard and soft responsive microswimmers. *Advanced Intelligent Systems* **2021**, *3* (4), 2000256.

(14) Villa, K.; Vyskočil, J.; Ying, Y.; Zelenka, J.; Pumera, M. Microrobots in Brewery: Dual Magnetic/Light-Powered Hybrid Microrobots for Preventing Microbial Contamination in Beer. *Chem.—Eur. J.* **2020**, *26* (14), 3039–3043.

(15) Peng, X.; Urso, M.; Ussia, M.; Pumera, M. Shape-controlled self-assembly of light-powered microrobots into ordered microchains for cells transport and water remediation. *ACS Nano* **2022**, *16* (5), 7615–7625.

(16) Xing, J.; Yin, T.; Li, S.; Xu, T.; Ma, A.; Chen, Z.; Luo, Y.; Lai, Z.; Lv, Y.; Pan, H.; et al. Sequential magneto-actuated and optics-triggered biomicrobots for targeted cancer therapy. *Adv. Funct. Mater.* **2021**, *31* (11), 2008262.

(17) Sun, Q.; Su, Q.; Gao, Y.; Zhou, K.; Song, W.; Quan, P.; Yang, X.; Ge, Z.; Zhang, Y.; He, G. Cationic telluroviologen derivatives as type-I photosensitizers for tumor photodynamic theranostics. *Aggregate* **2023**, *4* (3), No. e298.

(18) Guo, H.; Cao, Z.; Li, J.; Fu, Z.; Lin, S.; Wang, L.; Liu, J. Integrating bacteria with a ternary combination of photosensitizers for monochromatic irradiation-mediated photoacoustic imaging-guided synergistic photothermal therapy. *ACS Nano* **2023**, *17* (5), 5059–5071.

(19) Wang, J.; Gong, Q.; Jiao, L.; Hao, E. Research advances in BODIPY-assembled supramolecular photosensitizers for photodynamic therapy. *Coord. Chem. Rev.* **2023**, *496*, 215367.

(20) Zhang, H.; Li, Q.; Qi, X.; Li, Y.; Ma, H.; Grinholc, M.; Nakonieczna, J.; Yu, B.; Wang, X.; Zhang, L. Iron-blocking antibacterial therapy with cationic heme-mimetic gallium porphyrin photosensitizer for combating antibiotic resistance and enhancing photodynamic antibacterial activity. *Chemical Engineering Journal* **2023**, *451*, 138261.

(21) Irvani, S.; Varma, R. S. Plant pollen grains: A move towards green drug and vaccine delivery systems. *Nano-Micro Letters* **2021**, *13* (1), 128.

(22) Sanchez, S.; Solovev, A. A.; Mei, Y.; Schmidt, O. G. Dynamics of biocatalytic microengines mediated by variable friction control. *J. Am. Chem. Soc.* **2010**, *132* (38), 13144–13145.

(23) Ou, J.; Liu, K.; Jiang, J.; Wilson, D. A.; Liu, L.; Wang, F.; Wang, S.; Tu, Y.; Peng, F. Micro-/nanomotors toward biomedical applications: the recent progress in biocompatibility. *Small* **2020**, *16* (27), 1906184.

(24) Wang, X.; Fang, X.; Liu, X.; Lyu, Y.; Ma, L.; Fu, J. Spike nanoparticles: From design to biomedical applications. *Next Materials* **2024**, *2*, 100080.

(25) Dang, Z.; Sun, J.; Fan, J.; Li, J.; Li, X.; Chen, T. Zinc oxide spiky nanoparticles: A promising nanomaterial for killing tumor cells. *Materials Science and Engineering: C* **2021**, *124*, 112071.

(26) Dutta, S. D.; Hexiu, J.; Kim, J.; Sarkar, S.; Mondal, J.; An, J. M.; Lee, Y.-k.; Moniruzzaman, M.; Lim, K.-T. Two-photon excitable membrane targeting polyphenolic carbon dots for long-term imaging

- and pH-responsive chemotherapeutic drug delivery for synergistic tumor therapy. *Biomaterials Science* **2022**, *10* (7), 1680–1696.
- (27) Mundargi, R. C.; Potroz, M. G.; Park, J. H.; Seo, J.; Lee, J. H.; Cho, N.-J. Extraction of sporopollenin exine capsules from sunflower pollen grains. *RSC Adv.* **2016**, *6* (20), 16533–16539.
- (28) Barka-Bouaifel, F.; Sieber, B.; Bezzi, N.; Benner, J.; Roussel, P.; Boussekey, L.; Szunerits, S.; Boukherroub, R. Synthesis and photocatalytic activity of iodine-doped ZnO nanoflowers. *J. Mater. Chem.* **2019**, *21* (29), 10982–10989.
- (29) Hoogendoorn, B. W.; Birdsong, B. r. K.; Capezza, A. J.; Ström, V.; Li, Y.; Xiao, X.; Olsson, R. T. Ultra-low concentration of cellulose nanofibers (CNFs) for enhanced nucleation and yield of ZnO nanoparticles. *Langmuir* **2022**, *38* (41), 12480–12490.
- (30) Shah, E.; Mahapatra, P.; Bedekar, A. V.; Soni, H. P. Immobilization of *Thermomyces lanuginosus* lipase on ZnO nanoparticles: Mimicking the interfacial environment. *RSC Adv.* **2015**, *5* (33), 26291–26300.
- (31) Thongam, D. D.; Gupta, J.; Sahu, N. K. Effect of induced defects on the properties of ZnO nanocrystals: surfactant role and spectroscopic analysis. *SN Applied Sciences* **2019**, *1* (9), 1030.
- (32) Jayarambabu, N.; Kumari, B. S.; Rao, K. V.; Prabhu, Y. Germination and growth characteristics of mungbean seeds (*Vigna radiata* L.) affected by synthesized zinc oxide nanoparticles. *Int. J. Curr. Eng. Technol.* **2014**, *4* (5), 3411–3416.
- (33) Orji, B. O.; McDonald, A. G. Flow, curing and mechanical properties of thermoset resins-wood-fiber blends for potential additive-manufacturing applications. *Wood Material Sci. Eng.* **2023**, *18* (4), 1487–1504.
- (34) Sanaei-Rad, S.; Ghasemzadeh, M. A.; Aghaei, S. S. Synthesis and structure elucidation of ZnFe<sub>2</sub>O<sub>4</sub>/IRMOF-3/GO for the drug delivery of tetracycline and evaluation of their antibacterial activities. *J. Organomet. Chem.* **2022**, *960*, 122221.
- (35) Barick, K.; Nigam, S.; Bahadur, D. Nanoscale assembly of mesoporous ZnO: A potential drug carrier. *J. Mater. Chem.* **2010**, *20* (31), 6446–6452.
- (36) Wu, R.; Wang, H.; Hai, L.; Wang, T.; Hou, M.; He, D.; He, X.; Wang, K. A photosensitizer-loaded zinc oxide-polydopamine core-shell nanotherapeutic agent for photodynamic and photothermal synergistic therapy of cancer cells. *Chin. Chem. Lett.* **2020**, *31* (1), 189–192.
- (37) Li, Y.; Xu, H.; Li, H.; Zhong, S. Controlled preparation and photothermal properties of polydopamine microspheres. *Inorg. Chem. Commun.* **2021**, *124*, 108395.
- (38) Zhang, Z.; Yan, H.; Cao, W.; Xie, S.; Ran, P.; Wei, K.; Li, X. Ultrasound-Chargeable Persistent Luminescence Nanoparticles to Generate Self-Propelled Motion and Photothermal/NO Therapy for Synergistic Tumor Treatment. *ACS Nano* **2023**, *17* (16), 16089–16106.
- (39) Ran, F.; Ma, C.; Xiang, Y.; Xu, Y.; Liu, X.; Zhang, H. A fluorescent and colorimetric dual-channel sensor based on acid phosphatase-triggered blocking of internal filtration effect. *Microchimica Acta* **2021**, *188* (8), 282.
- (40) Villa, K.; Novotný, F.; Zelenka, J.; Browne, M. P.; Ruml, T. s.; Pumera, M. Visible-light-driven single-component BiVO<sub>4</sub> micromotors with the autonomous ability for capturing microorganisms. *ACS Nano* **2019**, *13* (7), 8135–8145.
- (41) Ussia, M.; Urso, M.; Dolezelikova, K.; Michalkova, H.; Adam, V.; Pumera, M. Active Light-Powered Antibiofilm ZnO Micromotors with Chemically Programmable Properties. *Adv. Funct. Mater.* **2021**, *31* (27), 2101178.
- (42) Mao, Z.; Peng, X.; Chen, H. Sunlight propelled two-dimensional nanorobots with enhanced mechanical damage of bacterial membrane. *Water Res.* **2023**, *235*, 119900.
- (43) Sun, M.; Chan, K. F.; Zhang, Z.; Wang, L.; Wang, Q.; Yang, S.; Chan, S. M.; Chiu, P. W. Y.; Sung, J. J. Y.; Zhang, L. Magnetic microswarm and fluoroscopy-guided platform for biofilm eradication in biliary stents. *Adv. Mater.* **2022**, *34* (34), 2201888.
- (44) Ji, X.; Yang, H.; Liu, W.; Ma, Y.; Wu, J.; Zong, X.; Yuan, P.; Chen, X.; Yang, C.; Li, X.; et al. Multifunctional parachute-like nanomotors for enhanced skin penetration and synergistic antifungal therapy. *ACS Nano* **2021**, *15* (9), 14218–14228.
- (45) Cui, T.; Wu, S.; Sun, Y.; Ren, J.; Qu, X. Self-propelled active photothermal nanoswimmer for deep-layered elimination of biofilm in vivo. *Nano Lett.* **2020**, *20* (10), 7350–7358.
- (46) Sun, J.; Zhang, P.; Fan, Y.; Zhao, J.; Niu, S.; Song, L.; Ma, L.; Ren, L.; Ming, W. Near-infrared triggered antibacterial nanocomposite membrane containing upconversion nanoparticles. *Materials Science and Engineering: C* **2019**, *103*, 109797.
- (47) Mendes, C. R.; Dilarri, G.; Forsan, C. F.; Sapata, V. d. M. R.; Lopes, P. R. M.; de Moraes, P. B.; Montagnolli, R. N.; Ferreira, H.; Bidoia, E. D. Antibacterial action and target mechanisms of zinc oxide nanoparticles against bacterial pathogens. *Sci. Rep.* **2022**, *12* (1), 2658.
- (48) Li, Y.; Chen, W.; Kang, Y.; Zhen, X.; Zhou, Z.; Liu, C.; Chen, S.; Huang, X.; Liu, H.-J.; Koo, S.; et al. Nanosensitizer-mediated augmentation of sonodynamic therapy efficacy and antitumor immunity. *Nat. Commun.* **2023**, *14* (1), 6973.
- (49) Erkoç, P.; Yasa, I. C.; Ceylan, H.; Yasa, O.; Alapan, Y.; Sitti, M. Mobile microrobots for active therapeutic delivery. *Advanced Therapeutics* **2019**, *2* (1), 1800064.
- (50) Gharpure, S.; Yadwade, R.; Ankamwar, B. Non-antimicrobial and non-anticancer properties of ZnO nanoparticles biosynthesized using different plant parts of *Bixa orellana*. *ACS omega* **2022**, *7* (2), 1914–1933.
- (51) Pandurangan, M.; Enkhtaivan, G.; Kim, D. H. Anticancer studies of synthesized ZnO nanoparticles against human cervical carcinoma cells. *Journal of Photochemistry and Photobiology B: Biology* **2016**, *158*, 206–211.
- (52) Efati, Z.; Shahangian, S. S.; Darroudi, M.; Amiri, H.; Hashemi, S. I.; Aghamaali, M. R. Green chemistry synthesized zinc oxide nanoparticles in *Lepidium sativum* L. seed extract and evaluation of their anticancer activity in human colorectal cancer cells. *Ceram. Int.* **2023**, *49* (20), 32568–32576.
- (53) Khalid, A. D.; Ur-Rehman, N.; Tariq, G. H.; Ullah, S.; Buzdar, S. A.; Iqbal, S. S.; Sher, E. K.; Alsaiani, N. S.; Hickman, G. J.; Sher, F. Functional bioinspired nanocomposites for anticancer activity with generation of reactive oxygen species. *Chemosphere* **2023**, *310*, 136885.
- (54) Peng, X.; Urso, M.; Balvan, J.; Masarik, M.; Pumera, M. Self-Propelled Magnetic Dendrite-Shaped Microrobots for Photodynamic Prostate Cancer Therapy. *Angew. Chem., Int. Ed.* **2022**, *61* (48), No. e202213505.
- (55) Mayorga-Martinez, C. C.; Fojtů, M.; Vyskočil, J.; Cho, N. J.; Pumera, M. Pollen-Based Magnetic Microrobots are Mediated by Electrostatic Forces to Attract, Manipulate, and Kill Cancer Cells. *Adv. Funct. Mater.* **2022**, *32* (46), 2207272.
- (56) Wang, X.; Cai, J.; Sun, L.; Zhang, S.; Gong, D.; Li, X.; Yue, S.; Feng, L.; Zhang, D. Facile fabrication of magnetic microrobots based on spirulina templates for targeted delivery and synergistic chemophotothermal therapy. *ACS Appl. Mater. Interfaces* **2019**, *11* (5), 4745–4756.
- (57) Ren, J.; Hu, P.; Ma, E.; Zhou, X.; Wang, W.; Zheng, S.; Wang, H. Enzyme-powered nanomotors with enhanced cell uptake and lysosomal escape for combined therapy of cancer. *Applied Materials Today* **2022**, *27*, 101445.
- (58) Sun, M.; Liu, Q.; Fan, X.; Wang, Y.; Chen, W.; Tian, C.; Sun, L.; Xie, H. Autonomous Biohybrid Urchin-Like Microperforator for Intracellular Payload Delivery. *Small* **2020**, *16* (23), 1906701.
- (59) Sun, M.; Fan, X.; Meng, X.; Song, J.; Chen, W.; Sun, L.; Xie, H. Magnetic biohybrid micromotors with high maneuverability for efficient drug loading and targeted drug delivery. *Nanoscale* **2019**, *11* (39), 18382–18392.
- (60) Zhang, H.; Li, Z.; Gao, C.; Fan, X.; Pang, Y.; Li, T.; Wu, Z.; Xie, H.; He, Q. Dual-responsive biohybrid neutroblots for active target delivery. *Science Robotics* **2021**, *6* (52), No. eaaz9519.
- (61) Huang, J.; Liu, Y.; Wu, J.; Dong, F.; Liu, C.; Luo, J.; Liu, X.; Wang, N.; Wang, L.; Xu, H. Extracellular Matrix-Mimicking Magnetic Microrobot for Targeted Elimination of Circulating Cancer Cells. *Nanoscale* **2024**, *16*, 624–634.

(62) Li, J.; Jiang, X.; Li, H.; Gelinsky, M.; Gu, Z. Tailoring materials for modulation of macrophage fate. *Adv. Mater.* **2021**, *33* (12), 2004172.

(63) Li, X.; Luo, S.; Chen, Y.; Zuo, Y.; Huang, Y.; Zhang, H.; Chen, L.; Feng, J.; Zhu, J.-Y.; Xue, W. Facile one-pot synthesis of meteor hammer-like Au-MnO<sub>x</sub> nanozymes with spiky surface for NIR-II light-enhanced bacterial elimination. *Chem. Mater.* **2022**, *34* (22), 9876–9891.

(64) Cockerill, I.; Su, Y.; Lee, J. H.; Berman, D.; Young, M. L.; Zheng, Y.; Zhu, D. Micro-/nanotopography on bioresorbable zinc dictates cytocompatibility, bone cell differentiation, and macrophage polarization. *Nano Lett.* **2020**, *20* (6), 4594–4602.